Rare Met. (2021) 40(6):1614–1621
https://doi.org/10.1007/s12598-020-01619-7

RARE METALS

ORIGINAL ARTICLE

Ultrathin CeO_2 nanosheets as bifunctional sensing materials for humidity and formaldehyde detection

Peng Zhang, Le-Xi Zhang*, Heng Xu, Yue Xing, Jing-Jing Chen, Li-Jian Bie*

Received: 29 June 2020 / Revised: 7 September 2020 / Accepted: 6 October 2020 / Published online: 14 November 2020

Abstract Issues like morphology control and further multifunctional applications are of significant importance for rare earth nano-oxides, e.g., cerium dioxide (CeO_2) nanostructures, however, relevant results in this respect are rather limited up to now. In the present work, ultrathin CeO_2 nanosheets were synthesized through a facile low-temperature hydrothermal method. The structure, morphology and specific surface area of these CeO_2 nanosheets were characterized by X-ray diffraction (XRD), field emission scanning electron microscope (FESEM) and N_2 adsorption–desorption. Significantly, CeO_2 nanosheets have the potential as bifunctional sensing materials to detect both humidity and formaldehyde vapor. The CeO_2 nanosheet humidity sensor exhibited excellent sensing characteristics in the relative humidity range of 11%–97% with the response value as high as 3.1×10^4. Meanwhile, the CeO_2 nanosheet gas sensor showed superior sensitivity and repeatability with fast response/recovery speed toward formaldehyde vapor at 300 °C. Finally, the humidity and formaldehyde sensing mechanism were discussed as well.

Keywords CeO_2 nanosheets; Humidity sensor; Gas sensor; Formaldehyde

1 Introduction

As one of the most important rare earth oxides, cerium dioxide (CeO_2) has been extensively studied over the past decades [1]. CeO_2 has been used prolifically in various applications, such as photocatalysis [2], water–gas shift [3], automobile exhaust-gas treatments [4], photocatalysts [5], adsorbents [6], and potential sensing applications [7, 8]. This widespread applicability mainly originates from the outstanding properties of CeO_2 [9], i.e., high oxygen storage capacity [10], quick and expedient mutation of the oxidation state between Ce^{4+} and Ce^{3+} [11], plentiful defects and high ionic mobility [12]. Therefore, based on the excellent performance of CeO_2 itself, researchers have started in-depth research on the synthesis and morphology regulation of cerium oxides [13]. A large number of studies showed that the morphology of CeO_2 has a great impact on its performance [14, 15]. The amelioration of CeO_2 performances was mainly focused on the preparation of nanoscale material or morphological change [16–18], such as nanotubes, nanowires, nanorods, nanocubes, nanopolyhedra, nanoplates, and nanosheets. Among them, nanosheets have attracted extensive attention in recent years due to their special morphology, larger specific surface area and more direct conduction pathways [19, 20]. Murray et al. reported a simple solution-phase synthetic method to prepare ultrathin CeO_2 nanosheets in the presence of

P. Zhang, L.-X. Zhang*, H. Xu, Y. Xing, J.-J. Chen, L.-J. Bie*
School of Materials Science and Engineering, Tianjin University of Technology, Tianjin 300384, China
e-mail: lxzhang@tjut.edu.cn; zhanglexi0318@126.com

L.-J. Bie
e-mail: ljbie@tjut.edu.cn; ljbie@pku.org.cn

P. Zhang, L.-X. Zhang, H. Xu, Y. Xing, J.-J. Chen, L.-J. Bie
Tianjin Key Laboratory for Photoelectric Materials and Devices, Tianjin 300384, China

P. Zhang, L.-X. Zhang, H. Xu, Y. Xing, J.-J. Chen, L.-J. Bie
Key Laboratory of Display Materials and Photoelectric Devices (Ministry of Education), Tianjin 300384, China

P. Zhang, L.-X. Zhang, H. Xu, Y. Xing, J.-J. Chen, L.-J. Bie
National Demonstration Center for Experimental Function Materials Education, Tianjin 300384, China

mineralizers [13]. Xie et al. synthesized ultrathin CeO_2 nanosheets using an intermediate precursor of $CeCO_3OH$ sheets [21]. However, the controllable synthesis of ultrathin CeO_2 nanosheets is still a challenge process, since the synthesis conditions are relatively complex [22], such as mineralizers required, surfactants needed, and high reaction temperature. Therefore, the development of simple and cost-effective processes for the synthesis of CeO_2 nanosheets is important to further explore their size- and shape-dependent properties.

In recent years, various CeO_2 nanomaterials have been utilized in highly efficient humidity sensors, such as nanoparticles [23], nanobelts [24], and aero-gel [25]. Additionally, CeO_2 nanostructures have been fully proved as active materials and additives/catalysts [26] for high-performance gas sensing applications, including nanospheres [7], nanopolyhedra [8], and nanoparticles [27]. Recently, research community focuses on metal oxide-based gas sensors operated at low temperature [28–30] or even room temperature [7, 27, 31] to reduce power consumption, simplify device architecture, etc. However, compared with that worked at conventional high temperatures (typically 200 °C–400 °C) [8, 26, 32], the room temperature gas sensors are commonly suffered from far lower response [7, 27] and much longer recovery time [7] for volatile organic compounds (VOCs) detection, especially formaldehyde [27]. For example, CeO_2 nanopolyhedra worked at 220 °C [8] exhibited much higher response (S_r = 12) toward 1×10^{-6} formaldehyde than that of CeO_2 nanoparticles operated at room temperature (S_r = 1.56) [27]. Therefore, it seems to be of significance to detect formaldehyde at high temperature for high and reversible response. Although great progresses have been made on CeO_2 synthesis and humidity/gas sensing properties, yet the bifunctional gas-humidity sensory applications of nano-CeO_2 have not been reported so far, the relative exploration of which can remarkably expand the application scope of CeO_2 materials.

Herein, ultrathin CeO_2 nanosheets were synthesized using a simple, one-step, inexpensive, low temperature and efficient hydrothermal method. Based on characterization and measurement, it was found that CeO_2 nanosheets can be used as potential bifunctional materials for humidity and formaldehyde detection. Finally, the excellent humidity and formaldehyde sensing mechanism were discussed as well.

2 Experimental

2.1 Synthesis of CeO_2 nanosheets

All reagents are analytical grade and used without further purification. In a typical synthesis, 2.5 mmol $Ce(NO_3)_3{\cdot}6H_2O$ was dissolved into 50 ml NaOH aqueous solution (6 $mol{\cdot}L^{-1}$), followed by stirring for 30 min. Then the mixed solution was moved into a 50 ml Teflon bottle and then sealed tightly in a stainless-steel autoclave. Hydrothermal treatment was carried out at 100 °C for 24 h. After the autoclave was cooled down to room temperature, the white precipitate was centrifugated, washed with distilled water several times, dried at 70 °C overnight. Finally, the dried yellow powders were annealed in air at 400 °C for 2 h.

2.2 Characterization

The structure was characterized by X-ray diffraction (XRD, D/Max 2500 pc) with a Cu Kα1 radiation (λ = 0.15406 nm) operating at 40 kV. The morphology was conducted by a field emission scanning electron microscope (FESEM, FEI Company, QUANTA FEG 250). The specific surface area was measured via the Brunauer-Emmett-Teller (BET) method using a N_2 adsorption at 77 K using a BELSORP-max apparatus.

2.3 Sensor fabrication and measurement

The assembly process of a planar humidity device based on CeO_2 nanosheets is introduced as follows. As-prepared CeO_2 nanosheets were mixed with water and ground into slurry, which was uniformly coated on an Al_2O_3 substrate (8 mm × 4 mm × 0.5 mm) with 5 pairs of Ag-Pd interdigitated electrodes (IDEs, electrode width and gap: 0.15 mm) to form a humidity sensor [33]. The humidity characteristic curves were measured on a CHS-1 Humidity Sensing Analysis System (Beijing Elite Tech. Co. Ltd., China) at room temperature (20 °C). The humidity sensing performance was examined at different RH conditions by adopting the method of saturated salt solutions. The humidity gradient was controlled by 6 jars (1 L) with rubber stoppers filled with different saturated salt solutions. The sensor in a shielded socket is sealed in a rubber stopper which is the same as that used for other jars. The tested ambient RH was achieved by saturated salt solutions in closed vessels, including LiCl (11%RH), $MgCl_2$ (33%RH), $Mg(NO_3)_2$ (54%RH), NaCl (75%RH), KCl (85%RH), and K_2SO_4 (97%RH). Before humidity sensing tests, 8 h stabilization of the jars was necessary to get fully liquid–gas equilibrium to ensure the RH accuracy. In a typical test cycle, the sensor was put in one jar until the impedance value achieved balance then it was switched to another one. After reaching steady, the sensor was taken back to the former jar waiting the next impedance stability, finally finishing a cyclic test. The humidity sensor response is defined as $S_{RH} = Z_{11\%}/Z_{RH}$, where $Z_{11\%}$ and Z_{RH} represent the impedance values of the humidity sensor taken at 11%RH and a detecting RH. The response time (τ_{res}) or

recovery time (τ_{rec}) is defined as the time duration needed for the sensor achieving 90% of total impedance change in the case of moisture adsorption or desorption, respectively.

The fabrication procedure of a CeO_2 based gas sensor is similar to our previous reports [20, 34]. The gas sensing properties of CeO_2 nanosheets were performed on a NS-4000 Smart Sensor Analyzer (Beijing Zhongke Micro-Nano Networking Technology Co. Ltd., China) with formaldehyde as the probe molecule. The gas sensor response is defined as $S_r = R_a/R_g$, where R_a and R_g are the resistances of the gas sensor in dry air and the target gas, respectively. The response time (τ_{res}) or recovery time (τ_{rec}) is defined as the time taken for the sensor output reaching 90% of its saturation after applying or switching off the gas in a step function.

3 Results and discussion

3.1 Material characterization

The XRD pattern (Fig. 1a) provides crystallinity and phase composition of as-prepared powders. All diffraction peaks can be well indexed to the standard diffraction data of the fluorite crystal structure CeO_2 (PDF No. 81-0792). No peak of any other impurities was detected, indicating the high purity of CeO_2. In addition, the broadening diffraction peaks indicate the nanoscale characteristic [20] of the CeO_2 sample. As shown in Fig. 1b, the internal structure of CeO_2 nanosheets was determined by N_2 adsorption–desorption isotherms. The curve shows a type-IV isotherm with an obvious hysteresis loop. This fact describes typical adsorption behavior of mesoporous materials via capillary condensation, which occurs between the desorption and the adsorption branch [35]. The BET specific surface area was calculated to be as high as 98.39 $m^2 \cdot g^{-1}$. As displayed in the inset of Fig. 1b, the pore size distribution using the BJH (Barrett-Joyner-Halenda) method indicates that the average mesopore diameter is 2.44 nm. The morphology of CeO_2 was recorded by FESEM. The low-magnification FESEM image (Fig. 1c) shows that CeO_2 powders are evenly distributed nanosheets with uniform size. As presented in the high-magnification FESEM image (Fig. 1d), the nanosheets are ~500 nm in length, ~150 nm in width, and ~10 nm in thickness. The unique morphology of ultrathin CeO_2 nanosheets is responsible for broadening diffraction peaks (Fig. 1a) and large specific surface area (Fig. 1b), these advantages of which imply a good candidate material for sensing applications.

3.2 Humidity sensing performance

In order to determine the optimum operating frequency (OOF), 10 Hz–100 kHz were selected to measure the

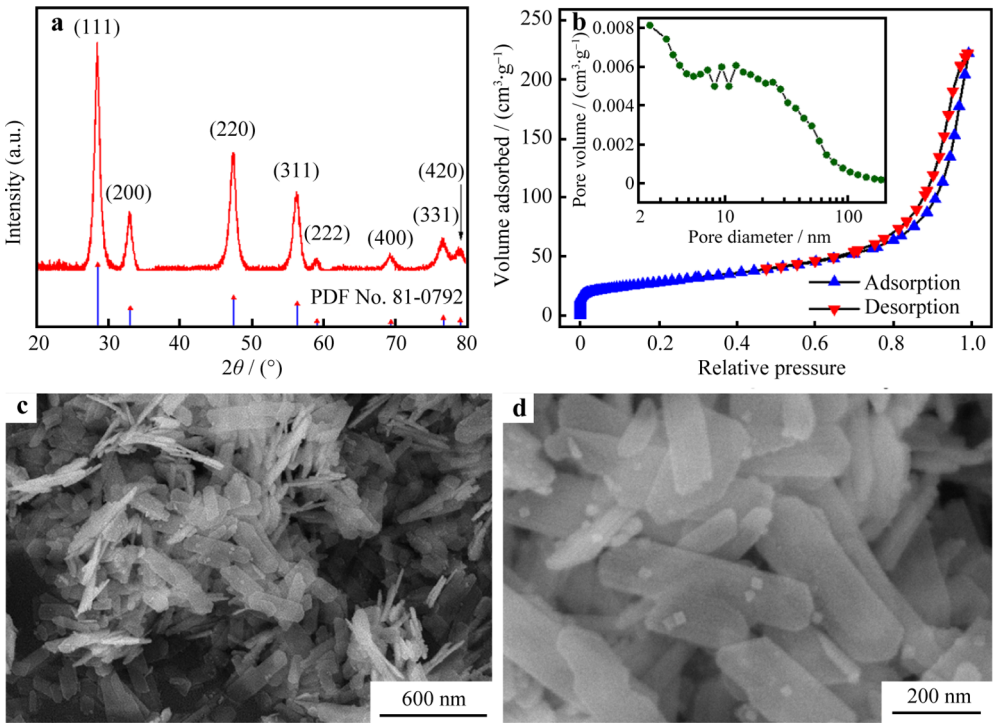

Fig. 1 **a** XRD pattern of CeO_2 nanosheets; **b** typical N_2 adsorption–desorption isotherms and pore size distribution plot (inset) of CeO_2 nanosheets; **c** low-magnification image and **d** enlarged FESEM image of CeO_2 nanosheets

frequency-dependent impedance of the humidity sensor at different RH levels at room temperature. As shown in Fig. 2a, it is obvious that the results of 100 Hz in the whole RH range have the highest response ($S_{97\%} = 3.1 \times 10^4$) and good linearity, so 100 Hz is adopted as the testing frequency. The response value of CeO_2 nanosheets is a lot higher than that of CeO_2 nanoparticles [23] and CeO_2 nanobelts [24], while nearly equal to that of CeO_2 aero-gel [25]. Figure 2b shows the impedance of the sensor alternate switching between 11%RH and 97%RH at 100 Hz. The back-and-forth exposure process between low RH and high RH can effectively demonstrate the excellent repeatability of the CeO_2 nanosheets sensor. The response time and recovery time have a great influence on the application of sensors. Figure 2c indicates the humidity sensor based on CeO_2 nanosheets enjoys a fast response time (11 s) and an acceptable recovery time (183 s). The response time of CeO_2 nanosheets is comparable to that of reported CeO_2 nanostructures [23–25], nevertheless the relatively longer recovery time needs further improvement. During the moisture adsorption–desorption process at 100 Hz (Fig. 2d), the maximum humidity hysteresis (ΔH_{max}) of the CeO_2 nanosheet sensor is only 2.1%RH. Interestingly to find that this value is smaller than or equal to that of some reported results of CeO_2 nanostructures [23–25]. This fact means that CeO_2 nanosheets possess excellent reversible sensing characteristics, which has the potential to be used as a high-performance material for humidity detection.

The conduction mechanism of humidity sensors can be effectively studied by complex impedance spectroscopy (CIS) and the corresponding equivalent circuit (EC). In Fig. 3a, at low humidity (11%RH), the impedance of CeO_2 nanosheets is very high, and the CIS basically seems like a straight line, which is actually an arc of a semicircle. The arc is related to the impedance of the electrode–electrolyte interface (Warburg impedance), because the intrinsic electrons of CeO_2 are the main carriers conducting electricity at relative low humidity. Since the relaxation time of ion diffusion is longer than that of charge transfer, the straight line can only be observed at high frequency [36, 37]. When RH gradually increases from 11% to 33% and then 54%, water molecules are physically absorbed on the surface of CeO_2 nanosheets, forming a discontinuous water layer and accelerating the transfer between H_2O and H_3O^+. At this time, the CIS presents a semicircle, and the impedance is still large, because CeO_2 nanosheets absorb only a few water molecules. Therefore, the EC at low RH,

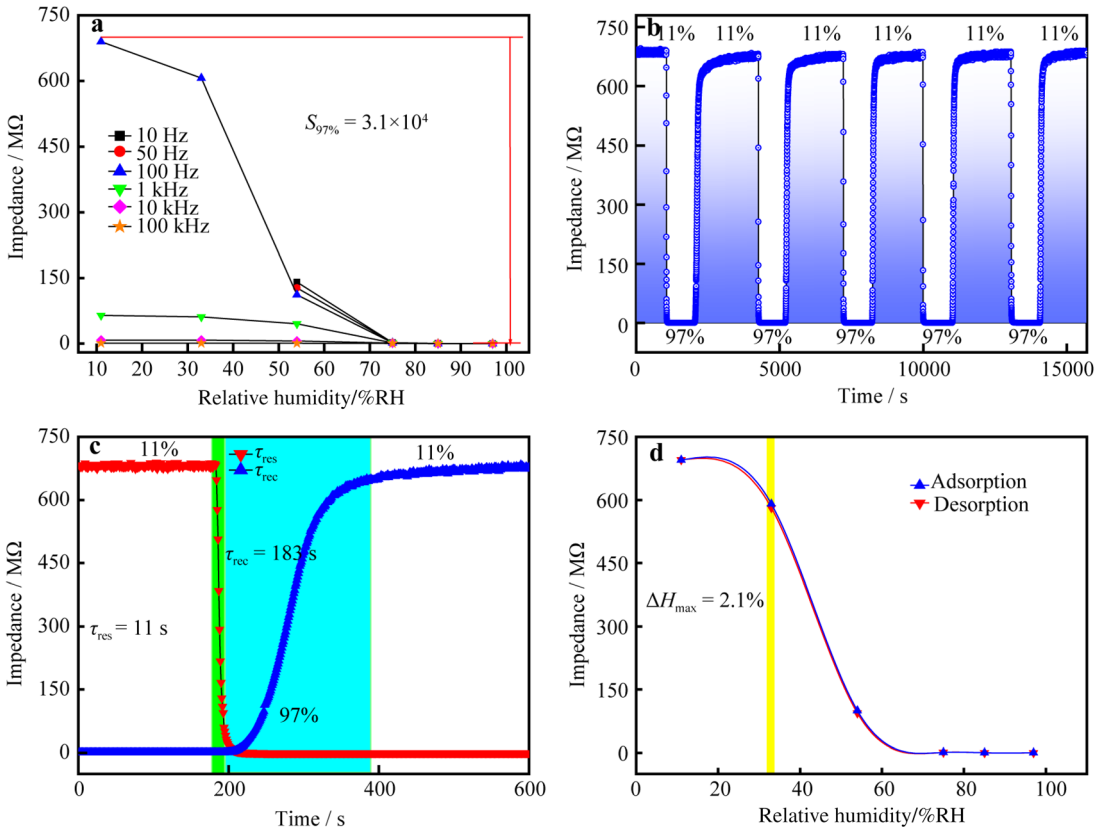

Fig. 2 **a** Impedance versus RH of CeO_2 nanosheet sensor at various frequencies; **b** repeatability of CeO_2 nanosheet sensor; **c** response and recovery time of humidity sensor; **d** hysteresis of humidity sensor at 100 Hz

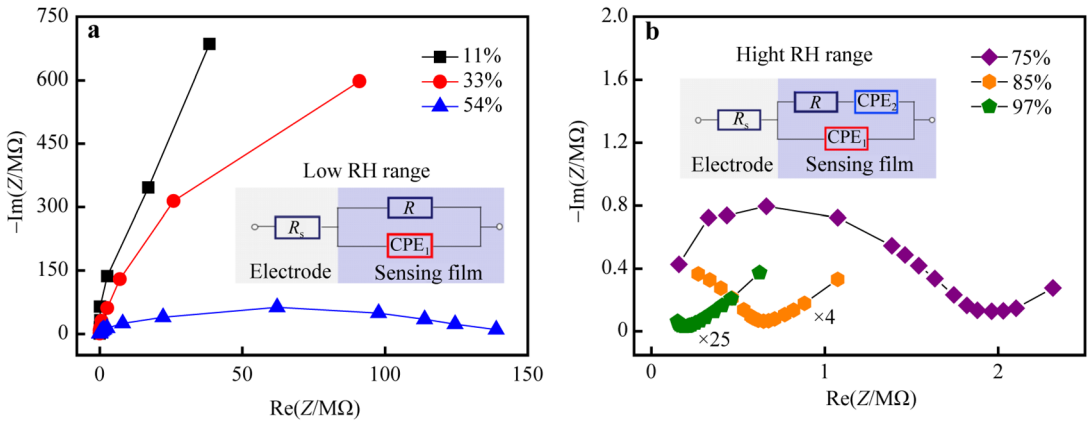

Fig. 3 Complex impedance plots and equivalent circuits (inset) of humidity sensor at **a** low RH range of 11%–54% and **b** high RH range of 75%–97%

as illustrated in the inset of Fig. 3a, is connected in series by two parts: one is the resistance (R_s), and the other part is the resistance (R) in parallel with the constant phase element (CPE_1). R_s is the electrode resistance, which is independent of RH. R and CPE_1 represent the resistances of the CeO_2 film and the role of H_3O^+ in the CeO_2 sensing layer.

When high RH is reached (75%, 85%, and 97%), the impedance of the sensor decreases with the increase of RH. As shown in Fig. 3b, the impedance diagram shows a semicircle and an oblique line, where the semicircle represents the inherent impedance of the sensor and the oblique line reveals the Warburg impedance [38]. In this process, water physically adsorbs on the surface of CeO_2, forming a continuous layer of water. The water layer acts as a channel for charge transfer and accelerates the transfer between H_2O and H_3O^+ [36], improving the conductivity of the CeO_2 nanosheet sensor. As shown in the inset of Fig. 3b, the EC is similar to that of the sensor at low RH (11%, 33%, and 54%). The difference is that the resistance of the sensing film is connected in series by the resistance (R) and the constant phase element (CPE_2). The straight line at the low frequency of CIS can also be represented by the constant phase element (CPE_1), which describes that H_3O^+ influences the physisorbed water layer through the jumping of H^+ between adjacent water molecules.

3.3 Gas sensing performance

Gas sensors based on semiconducting metal oxides (SMO) usually exhibit the best response values at a certain temperature, because SMO can be well thermally activated at this temperature. Figure 4a shows the response of the CeO_2 based gas sensor to 200×10^{-6} formaldehyde at different operating temperatures. Obviously, 300 °C is selected as the optimal operating temperature (OOT) of the gas sensor, and the response to 200×10^{-6} formaldehyde is up to 30 at this temperature. As represented in Fig. 4a (right Y axis), the resistance of CeO_2 nanosheets in air (R_a) decreases with the increase of operating temperature, indicating a characteristic semiconducting behavior. Meanwhile, selectivity is an important parameter to evaluate the potential application of gas sensing materials. As shown in Fig. 4b, various typical VOCs likely to be presented in indoor environments are selected as interfering gases to test the selectivity at a fixed concentration (200×10^{-6}) at 300 °C, such as halogenated hydrocarbon (trichloromethane, $CHCl_3$), ketone (acetone, CH_3COCH_3), aromatic hydrocarbons (benzene, C_6H_6; toluene, C_7H_8), and organic amine (methylamine, CH_3NH_2). Obviously, the gas sensor exhibits the highest response value and thus good selectivity to formaldehyde. The gas sensor presents extremely fast response time (20 s) and recovery time (10 s) toward 200×10^{-6} formaldehyde at 300 °C, as can be seen in Fig. 4c. Meanwhile, the gas sensor performs well in repetitive test cycles (Fig. 4d). Figure 4e shows the response of the gas sensor exposed to different concentrations of formaldehyde in turn at 300 °C exhibited in response (left Y axis) and resistance (right Y axis), indicating good dynamic response-recovery performance. When the formaldehyde concentration reaches 200×10^{-6} and above, the response of the sensor does not change much, implying saturation response. This phenomenon follows the Langmuir–Hinshelwood mechanism that is correspondence with the larger specific surface area (Fig. 1b), and the sensor surface coverage tends to be saturated at higher concentrations than 200×10^{-6}. In Fig. 4f, the fitted function interprets the relationship between S_r and concentration (C) of the CeO_2 nanosheet sensor, enjoying a good relativity (adjust $R^2 = 0.9854$). Compared with other formaldehyde sensors based on CeO_2 nanomaterials [8, 27], as-synthesized CeO_2 nanosheet

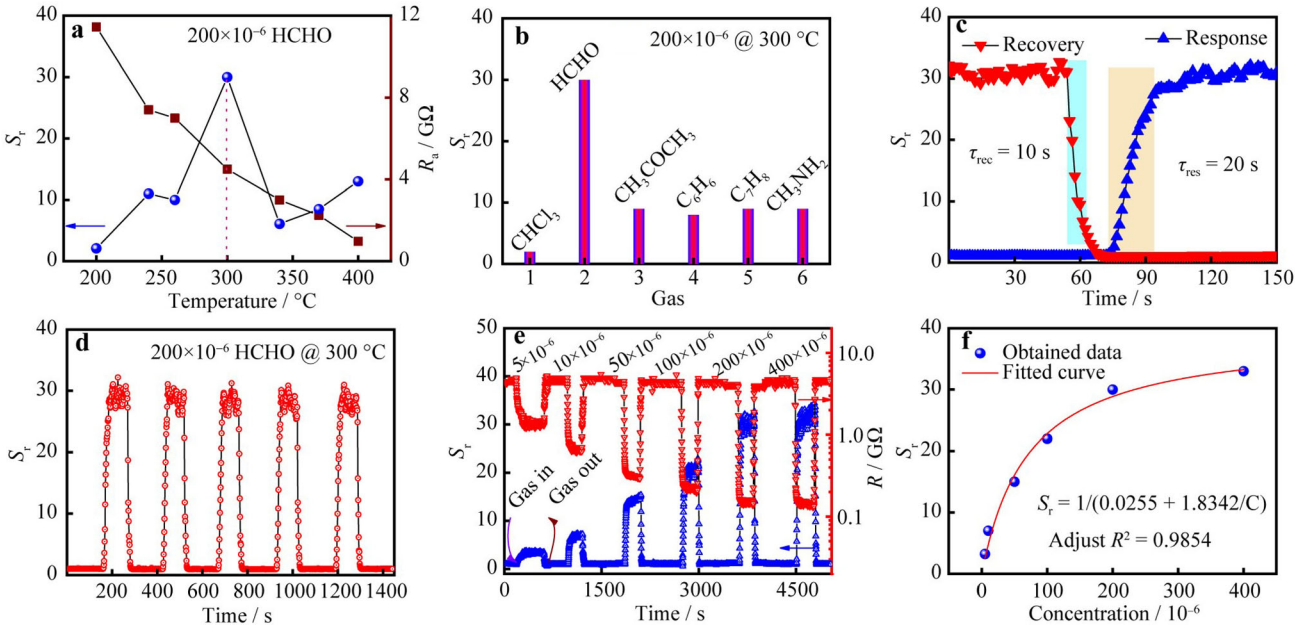

Fig. 4 **a** Response in 200 × 10^{-6} formaldehyde (left *Y* axis) and resistance in air (right *Y* axis) of CeO_2 nanosheets at different operation temperatures; **b** selectivity of CeO_2 nanosheets toward 200 × 10^{-6} gases at 300 °C; **c** response-recovery curves and **d** repeatability of CeO_2 nanosheets toward 200 × 10^{-6} formaldehyde at 300 °C; **e** dynamic response-recovery curve of CeO_2 nanosheets exposed to 5 × 10^{-6}–400 × 10^{-6} formaldehyde at 300 °C exhibited in response (left *Y* axis) and resistance (right *Y* axis), respectively; **f** fitted curve (solid line) and experimental results (scattered points) of CeO_2 nanosheets to 5 × 10^{-6}–400 × 10^{-6} formaldehyde at 300 °C

sensor holds favorable gas sensing performance, including high response, fast response-recovery, good repeatability and selectivity, while a higher operating temperature. All these results indicate that the sensor based on ultrathin CeO_2 nanosheets is of practical significance to detect formaldehyde vapor.

As depicted in Fig. 5, electron depletion theory is accepted to explain the gas sensing mechanism. This mechanism refers to a drastic resistance change of a SMO based gas sensor (CeO_2 here) via the adsorption-oxidization-desorption process toward reducing gas (formaldehyde in this work) [39]. In air, oxygen molecules are absorbed on the surface of CeO_2, and capture electrons from the CeO_2 conduction band (CB) to form oxygen species (O_2^-, O^- and O^{2-}) at different temperatures [40]. Thus, an electron depletion layer occurs on CeO_2 surface, resulting in a high resistance state of CeO_2 (R_a). Once exposed to formaldehyde, oxygen species oxidize formaldehyde and electrons trapped in the adsorbed state are released, leading to increased carrier concentration, narrower depletion layer and finally reduced sensor resistance (R_g) [41]. In this work, the superior gas sensing performance of CeO_2 nanosheets, especially the high response value and short response-recovery time, is originated from the combined effects of large specific surface area, characteristically small thickness, and unique mesoporous architecture.

4 Conclusion

In summary, ultrathin CeO_2 nanosheets were synthesized by a facile low-temperature hydrothermal method. These CeO_2 nanosheets were investigated as bifunctional sensing materials for humidity and formaldehyde detection for the

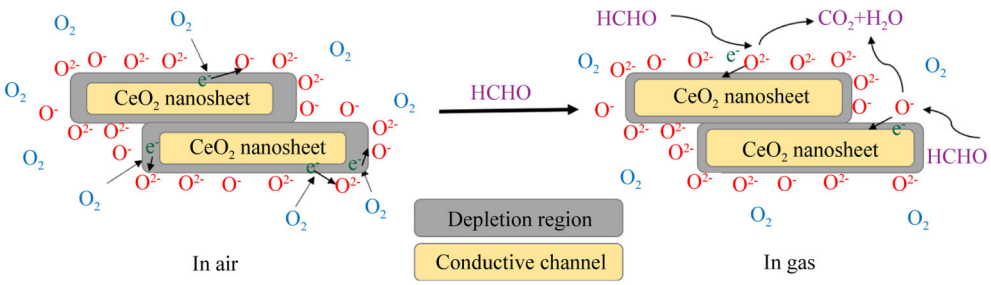

Fig. 5 Schematic illustration of sensing mechanism of CeO_2 nanosheets in air and formaldehyde

first time. The humidity sensor based on CeO_2 nanosheets possesses impedance change larger than 4 orders of magnitude ($S_{97\%} = 3.1 \times 10^4$), short response-recovery times (20 and 10 s), and narrow hysteresis (2.1%RH). Simultaneously, the gas sensor based on CeO_2 nanosheets holds high sensitivity, fast response, good repeatability and selectivity to 5×10^{-6}–400×10^{-6} formaldehyde at 300 °C. It is believed that the excellent bifunctional sensing performance can be attributed to the geometric sensitization of ultrathin CeO_2 nanosheets. This work provides a good candidate material for both humidity and formaldehyde detection, and furthermore, suggests a new way for the design and synthesis of other rare earth oxides for multifunctional applications.

Acknowledgements This work was financially supported by the National Natural Science Foundation of China (Nos. 21601094 and 21401139), the Natural Science Foundation of Tianjin City (Nos. 15JCQNJC02900 and 18JCQNJC73900) and Tianjin Municipal Education Commission (No. 2018KJ130).

References

[1] Montini T, Melchionna M, Monai M, Fornasiero P. Fundamentals and catalytic applications of CeO_2-based materials. Chem Rev. 2016;116(10):5987.

[2] Wu M, Zhang Y, Szeto W, Pan W, Huang H, Leung DYC. Vacuum ultraviolet (VUV)-based photocatalytic oxidation for toluene degradation over pure CeO_2. Chem Eng Sci. 2019;200:203.

[3] Si R, Flytzani-Stephanopoulos M. Shape and crystal-plane effects of nanoscale ceria on the activity of Au-CeO_2 catalysts for the water-gas shift reaction. Angew Chem Int Edit. 2008;47(15):2884.

[4] Sayle DC, Maicaneanu SA, Watson GW. Atomistic models for CeO_2(111), (110), and (100) nanoparticles, supported on yttrium-stabilized zirconia. J Am Chem Soc. 2002;124(38):11429.

[5] Ferraz NP, Nogueira AE, Marcos FCF, Machado VA, Rocca RR, Assaf EM, Asencios YJO. CeO_2–Nb_2O_5 photocatalysts for degradation of organic pollutants in water. Rare Met. 2020;39(3):230.

[6] Pang JH, Liu Y, Li J, Yang XJ. Solvothermal synthesis of nano-CeO_2 aggregates and its application as a high efficient arsenic adsorbent. Rare Met. 2019;38(1):73.

[7] Zito CA, Perfecto TM, Volanti DP. Porous CeO_2 nanospheres for room temperature triethylamine sensor under high humidity condition. New J Chem. 2018;42:15954.

[8] Hussain S, Aslam N, Yang XY, Javed MS, Xu ZW, Wang MS, Liu GW, Qiao GJ. Unique polyhedron CeO_2 nanostructures for superior formaldehyde gas-sensing performances. Ceram Int. 2018;44(16):19624.

[9] Zou W, Deng B, Hu X, Zhou Y, Pu Y, Yu S, Ma K, Sun JF, Wan HQ, Dong L. Crystal-plane-dependent metal oxide-support interaction in CeO_2/g-C_3N_4 for photocatalytic hydrogen evolution. Appl Catal B Environ. 2018;238:111.

[10] Zhang J, Kumagai H, Yamamura K, Ohara S, Takami S, Morikawa A, Shinjoh H, Kaneko K, Adschiri T, Suda A. Extra-low-temperature oxygen storage capacity of CeO_2 nanocrystals with cubic facets. Nano Lett. 2011;11(2):361.

[11] Grabchenko MV, Mamontov GV, Zaikovskii VI, La Parola V, Liotta LF, Vodyankina OV. The role of metal-support interaction in Ag/CeO_2 catalysts for CO and soot oxidation. Appl Catal B Environ. 2020;260:16.

[12] Huang WX, Gao YX. Morphology-dependent surface chemistry and catalysis of CeO_2 nanocrystals. Catal Sci Technol. 2014;4(11):3772.

[13] Wang DY, Kang YJ, Doan-Nguyen V, Chen J, Kungas R, Wieder NL, Bakhmutsky K, Gorte RJ, Murray CB. Synthesis and oxygen storage capacity of two-dimensional ceria nanocrystals. Angew Chem Int Edit. 2011;50(19):4378.

[14] Cao T, You R, Li ZR, Zhang XY, Li D, Chen SL, Zhang ZH, Huang WX. Morphology-dependent CeO_2 catalysis in acetylene semihydrogenation reaction. Appl Surf Sci. 2020;501:13.

[15] Tan HY, Wang J, Yu SZ, Zhou KB. Support morphology-dependent catalytic activity of Pd/CeO_2 for formaldehyde oxidation. Environ Sci Technol. 2015;49(14):8675.

[16] Sun CW, Li H, Chen LQ. Nanostructured ceria-based materials: synthesis, properties, and applications. Energy Environ Sci. 2012;5(9):8475.

[17] Zhang DS, Fu HX, Shi LY, Fang JH, Li Q. Carbon nanotube assisted synthesis of CeO_2 nanotubes. J Solid State Chem. 2007;180(2):654.

[18] Padmanathan N, Selladurai S. Shape controlled synthesis of CeO_2 nanostructures for high performance supercapacitor electrodes. RSC Adv. 2014;4(13):6527.

[19] Yu H, Yang TY, Zhao R, Xiao BX, Li ZF, Zhang MZ. Fast formaldehyde gas sensing response properties of ultrathin SnO_2 nanosheets. RSC Adv. 2015;5(126):104574.

[20] Xu R, Zhang LX, Li MW, Yin YY, Yin J, Zhu MY, Chen JJ, Wang Y, Bie LJ. Ultrathin SnO_2 nanosheets with dominant high-energy 001 facets for low temperature formaldehyde gas sensor. Sens Actuat B Chem. 2019;289:186.

[21] Sun YF, Liu QH, Gao S, Cheng H, Lei FC, Sun ZH, Jiang Y, Su HB, Wei SQ, Xie Y. Pits confined in ultrathin cerium (IV) oxide for studying catalytic centers in carbon monoxide oxidation. Nat Commun. 2013;4:2899.

[22] Xu J, Chen XY, Xu YS, Du YP, Yan CH. Ultrathin 2D rare-earth nanomaterials: compositions, syntheses, and applications. Adv Mater. 2020;32(3):1806461.

[23] Thakur S, Patil P. Rapid synthesis of cerium oxide nanoparticles with superior humidity-sensing performance. Sens. Actuat B Chem. 2014;194:260.

[24] Wang C, Wang Y. Effects of different surfactants on humidity sensing properties of CeO_2 nanobelts thin film prepared by hydrothermal method. Int J Appl Ceram Technol. 2015;12:E142.

[25] Poonia E, Mishra PK, Kiran V, Sangwan J, Kumar R, Rai PK, Malik R, Tomer VK, Ahuja R, Mishra YK. Aero-gel based CeO_2 nanoparticles: synthesis, structural properties and detailed humidity sensing response. J Mater Chem C. 2019;7:5477.

[26] Wang D, Yin Y, Xu P, Wang F, Wang P, Xu J, Wang X, Li X. Catalytic-induced sensing effect of triangular CeO_2 nanoflakes for enhanced BTEX vapor detection with conventional ZnO gas sensors. J Mater Chem A. 2020;8:11188.

[27] Pandeeswari R, Jeyaprakash BG. CeO_2 thin film as a low-temperature formaldehyde sensor in mixed vapour environment. Bull Mater Sci. 2014;37(6):1293.

[28] Wan K, Wang D, Wang F, Li H, Xu J, Wang X, Yang J. Hierarchical In_2O_3@SnO_2 core–shell nanofiber for high efficiency formaldehyde detection. ACS Appl Mater Interfaces. 2019;11(48):45214.

[29] Su C, Zhang L, Han Y, Chen X, Wang S, Zeng M, Hu N, Su Y, Zhou Z, Wei H, Yang Z. Glucose-assisted synthesis of hierarchical flower-like Co_3O_4 nanostructures assembled by porous nanosheets for enhanced acetone sensing. Sens Actuat B Chem. 2019;288:699.

[30] Su C, Zhang L, Han Y, Ren C, Chen X, Hu J, Zeng M, Hu N, Su Y, Zhou Z, Yang Z. Controllable synthesis of crescent-shaped porous NiO nanoplates for conductometric ethanol gas sensors. Sens Actuat B Chem. 2019;296:126642.
[31] Han Y, Ma Y, Liu Y, Xu S, Chen X, Zeng M, Hu N, Su Y, Zhou Z, Yang Z. Construction of MoS_2/SnO_2 heterostructures for sensitive NO_2 detection at room temperature. Appl Surf Sci. 2019;493:613.
[32] Yuan Z, Han E, Meng F, Zuo K. Detection and identification of volatile organic compounds based on temperature-modulated ZnO sensors. IEEE T Instrum Meas. 2020;69(7):4533.
[33] Liu L, Zhang C, Zhang LX, Li Q, Yin YY, Wang HY, Sun RH, Li JY, Hou XY, Dong H, Bie LJ. A 2D coordination polymer of $[Cd(TMA)(4\text{-}CNPy)(H_2O)]_n$ (H_2TMA = 3-thiophenemalonic acid, 4-CNPy = 4-cyanopyridine) with impedimetric humidity sensing performance. Inorg Chem Commun. 2020;111:107636.
[34] Qiao PY, Zhang LX, Zhu MY, Yin YY, Zhao ZW, Sun HN, Dong JY, Bie LJ. Acetylene sensing enhancement of mesoporous ZnO nanosheets with morphology and defect induced structural sensitization. Sens Actuat B Chem. 2017;250:189.
[35] Alghouti MA, Da'ana DA. Guidelines for the use and interpretation of adsorption isotherm models: a review. J Hazard Mater. 2020;393:22.
[36] Yu SG, Zhang HY, Chen C, Lin CC. Investigation of humidity sensor based on Au modified ZnO nanosheets via hydrothermal method and first principle. Sens Actuat B Chem. 2019;287:526.
[37] Wang Z, Lu Y, Yuan S, Shi L, Zhao Y, Zhang M, Deng W. Hydrothermal synthesis and humidity sensing properties of size-controlled zirconium oxide (ZrO_2) nanorods. J Colloid Interface Sci. 2013;396:9.
[38] Zhang DZ, Liu JJ, Xia BK. Layer-by-layer self-assembly of zinc oxide/graphene oxide hybrid toward ultrasensitive humidity sensing. IEEE Electr Device L. 2016;37(7):916.
[39] Song HJ, Yan SW, Yao YL, Xia LX, Jia XH, Xu JS. 3D α-Fe_2O_3 nanorods arrays@graphene oxide nanosheets as sensing materials for improved gas sensitivity. Chem Eng J. 2019;370:1331.
[40] Ma JW, Fan HQ, Zhang WM, Sui JN, Wang C, Zhang MC, Zhao N, Yadav AK, Wang WJ, Dong WQ, Wang SR. High sensitivity and ultra-low detection limit of chlorine gas sensor based on In_2O_3 nanosheets by a simple template method. Sens Actuat B Chem. 2020;305:127456.
[41] Chen T, Liu QJ, Zhou ZL, Wang YD. The fabrication and gas-sensing characteristics of the formaldehyde gas sensors with high sensitivity. Sens Actuat B Chem. 2008; 131(1):301.